Journal of the European Ceramic Society 16 (1996) 177–186

0955-2219(95)00149-2
0955-2219/96/$15.00

Interpretation of Mullite Real Structure via Inter-vacancy Correlation Vectors

S. H. Rahman,[a] S. Strothenk,[a] C. Paulmann[b] & U. Feustel[a]

[a]Institut für Mineralogie, Universität Hannover, Welfengarten 1, 30167 Hannover, Germany
[b]Mineralogisch-Petrographisches Institut, Universität Hamburg, Grindelallee 48, 20146 Hamburg, Germany

(Accepted 22 July 1995)

Abstract

High resolution electron microscopy (HREM) results yield that the oxygen vacancies in mullite form domains with higher oxygen vacancy concentrations and specific preferred directions. The domains are more or less statistically distributed in a disordered matrix. In the (0 1 0) plane the oxygen vacancies are arranged along [1 0 2] and [1 0 –2] over two to four unit cells. In addition, ordered domains with higher amounts of vacancies exhibit a doubling of the c*-axis which can already be seen in* h 0 l *diffraction patterns. Vacancy arrangements in the (1 0 0) plane are characterized by preferred orientations along [0 1 2] and [0 1 –2] and [0 0 1], resulting in an average direction parallel to [0 1 3] and [0 1 –3]. Columns with higher vacancy concentrations usually reveal distances of 1·5*b *and 5 to 6*c.

Considering the above-mentioned HREM results, the real structure configuration of 2 : 1 mullite has been established using the videographic two-dimensional and three-dimensional simulation method. The ordering scheme of the oxygen vacancies can be described via inter-vacancy correlation vectors (short-range order vectors l m n; l = a*/2,* m = b*/2),* n = c*). It has been confirmed that the inter-vacancy correlation vectors <1 1 1>, <2 0 1> and <3 1 0> are preferred but a complete structure description can only be obtained by considering the correlation vectors <0 2 2>, <3 3 0>, <1 3 0>, <4 0 1>, <1 1 3>, <0 4 0>, <2 2 2>, <2 2 3>, <6 0 0> and <3 1 2> additionally. These inter-vacancy vectors, especially <0 2 2> and <3 3 0>, play an important role for the formation of the diffuse scattering in the* h 0 l *and* 0 k l *plane.*

Introduction

Deviations from the ideal periodic arrangement (point defects, modulations, short-range order, domain boundaries, etc.) strongly influence the physical properties of crystalline solids. Hence, determination of the real structure becomes a major task in examining the influence of structural disorder on the physical behaviour of materials.

Characteristic features in diffraction patterns of disordered crystals are diffuse scattering and/or satellite reflections apart from the Bragg reflections, the latter being attributed to the average structure. Diffuse scattering, caused by short-range ordering, cannot be directly interpreted by known structural disorder theories[1,2] which mainly deal with discrete satellite reflections. However, Monte Carlo methods in conjunction with optical or computer-based Fourier transforms yield information about deviations from the average structure. Besides this, high resolution electron microscopy (HREM) in combination with contrast simulations of predefined structure models is the most important real space method to achieve information about certain types of structural disorder on the atomic scale.

The above-mentioned methods have been applied to characterize the ordering phenomena of oxygen vacancies in the non-stoichiometric aluminosilicate mullite ($Al_2[Al_{2+2x}Si_{2-2x}]O_{10-x}$) which shows a complex scheme of satellite reflections and diffuse scattering throughout reciprocal space (Fig. 1).

HREM investigations of mullite mainly deal with beam directions parallel to [0 0 1][3–7] and [0 1 0].[8–10] Recently, Paulmann *et al.*[11] performed 200 kV and 300 kV HREM investigations along [0 1 0] and [1 0 0]. They found preferred vacancy orientations in domains with higher vacancy concentrations, distributed in a matrix with minor degree of order.

Early investigations of the satellite reflections with optical Fourier transforms were performed by Saalfeld[12] for the $h0l$ plane. Tokonami *et al.*[13] examined the diffuse scattering in $hk\frac{1}{2}$ and $hk\frac{2}{9}$ planes and derived a model of the vacancy arrangement in large domains. Monte Carlo simulations of structural models together with their Fourier transforms were presented by Welberry

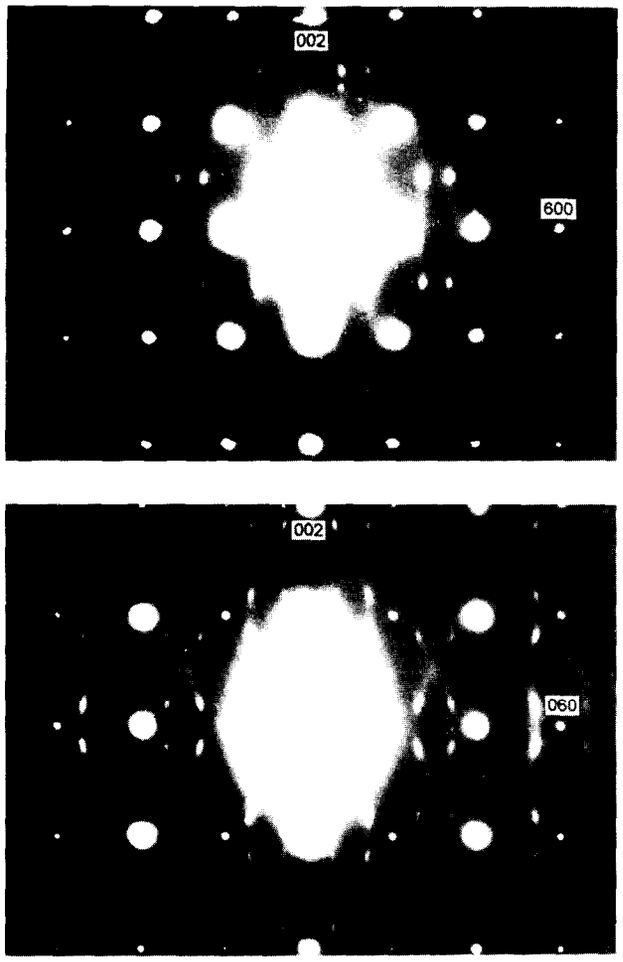

Fig. 1. Electron diffraction patterns of mullite: top, $h0l$; bottom, $0kl$.

and Withers[14] to explain the diffuse scattering in $hk\frac{1}{6}$, $hk\frac{1}{4}$, $hk\frac{1}{3}$, $hk\frac{1}{2}$.

Taking the results of HREM investigations into consideration, a specific distribution scheme of inter-vacancy vectors in the (0 0 1) plane was presented by Rahman,[15,16] Rahman and Paulmann,[17] Paulmann *et al.*[18] and Paulmann *et al.*[11] Butler *et al.*[19] recently carried out a three-dimensional (3-D) real structure simulation by taking interaction pair energies into account, the latter having been obtained by Padlewski *et al.*[20] Variation and addition of pair energies led to relatively good agreement of Fourier transforms with the experimental diffraction patterns of the $hk\frac{1}{3}$ and $hk\frac{1}{2}$ reciprocal planes, whereas the Fourier transforms for $hk\frac{1}{6}$ and $hk\frac{1}{4}$ differed slightly from the experimental patterns.

Until now, Monte Carlo simulations of the mullite real structure have mostly dealt with the diffuse scattering in reciprocal planes from $hk0$ to $hk\frac{1}{2}$, taking neither the position of satellite reflections nor the diffuse scattering in $h0l$ and $0kl$ diffraction patterns into account. Additionally, no next nearest inter-vacancy correlation vectors were considered,[21] although these vectors may play an important role in the exact interpretation of the additional diffraction phenomena in the $h0l$ and $0kl$ planes.

Consequently, the aim of the present study is to combine results from a quantitative investigation of HREM images by contrast simulations and digital image processing methods with videographic real structure simulations[22] to receive a 3-D description of the oxygen vacancy arrangement in mullite via inter-vacancy correlation vectors.

Experimental

The investigated specimens of 2:1 mullite grew as single crystals (3 × 3 × 10 mm) in ingots of commercially produced mullite bricks which were synthesized by heating a mixture of kaolinite and Al_2O_3 with an arc furnace and casting the melt at 2000°C. Several microprobe analyses of crystals with well-developed {1 1 0} faces and growth direction along [0 0 1] gave a chemical composition of 75·9 wt% Al_2O_3 and 23·8 wt% SiO_2 (x = 0·39), close to the ideal value of 0·40.

Electron microscope investigations (diffraction, HREM) were performed using Hitachi H-800 and H-9000 microscopes with LaB_6 cathodes, operating at 200 and 300 kV accelerating voltage, respectively.

Preparation of crystallites was carried out by conventional crushing with propanol in an agate mortar and transferring the suspension to carbon-coated copper grids.

The computer system for videographic real structure simulations comprised of an IBM-AT with a special array processor and graphic adaptor boards interconnected by a fast external port and to the host computer through the AT-bus interface. The configuration permitted calculation of fast Fourier transforms (FFT) of 1024 × 1024 pixels and 8-bit colour depth within 8 s.

HREM Investigations

HREM investigations of real structures require contrast simulations with predefined structure models to permit a correct interpretation of the contrast patterns. A detailed study with beam directions along [0 1 0] and [1 0 0] was recently carried out by Paulmann *et. al.*[11] since the satellite reflections, indicating an incommensurate modulation of the mullite structure, are best visible in $h0l$ and $0kl$ diffraction patterns. A projection of the structure along these directions shows a dense packing of atoms with different scattering potentials. Nevertheless, extensive contrast simulations of supercells with more than 2000 atoms revealed

striking changes of the contrast pattern in the immediate vicinity of projected vacancy positions. This fact can be attributed to associated cation shifts near an oxygen vacancy which result in a remarkable change of the scattering potential. Both planes are characterized by contrast enhancements at vacancy positions, whereas in the (0 0 1) plane[4] an intensity decrease of dots located clockwise next to a vacancy position is observed. Through-focus series of the (0 1 0) and (1 0 0) planes gave characteristic defect-induced contrast patterns at defocus values of –30, –65, –75 nm and –35, –45, –65, –75 nm, respectively. More details about the applied supercells and simulation parameters are given elsewhere.[11,16] Special attention should be paid to a defocus range of –25 to –35 nm where dots in the contrast pattern directly coincide with the vacancy position (*ac*-plane) or cause an elongated and enhanced dot (*bc*-plane).

Figure 2 shows 200 kV HREM images along [0 1 0] and [1 0 0] at approximate defocus values of –30 nm. Closer inspection of the images reveals intensity variations of dots which can be attributed to higher vacancy concentrations along the incident beam.[11] Further investigations with different vacancy concentrations and different arrangements yield a linear dependence of defect-induced intensity enhancements and the concentration of oxygen vacancies along the beam direction. Furthermore, concentrations of only 20% still cause a detectable change of the contrast pattern.

In order to determine preferred vacancy arrangements in the (0 1 0) and (1 0 0) planes, digitized HREM images were investigated by image processing methods. After determining the greyscale area of the contrast patterns (8 bit) in Fig. 2, a progressive filtering procedure of selected greyscale areas was performed. As the stepwise filtering progresses, a continuous decrease of the observable maxima can be detected [Figs 3(a)–(e) and 4(a)–(e)], which enables the determination of O_c columns with different concentrations of vacancies and domains with specific ordering schemes. Detailed analyses were carried out for selected areas [rectangles in Figs 3(a) and 4(a)] and the results are presented in Figs 3(f) and 4(f), respectively.

A striking feature of (0 1 0) HREM images are linear arrangements of higher vacancy concentrations along [1 0 2] and [1 0 –2] over two to four unit cells. In addition, ordered domains with higher amounts of vacancies exhibit a doubling of the *c*-axis which can already be seen in *h* 0 *l* diffraction patterns. Combining the arrangements along [1 0 2] and [1 0 –2] and the twofold periodicity along [0 0 1] yields a centred pattern with columns of higher oxygen vacancy concentrations, frequently

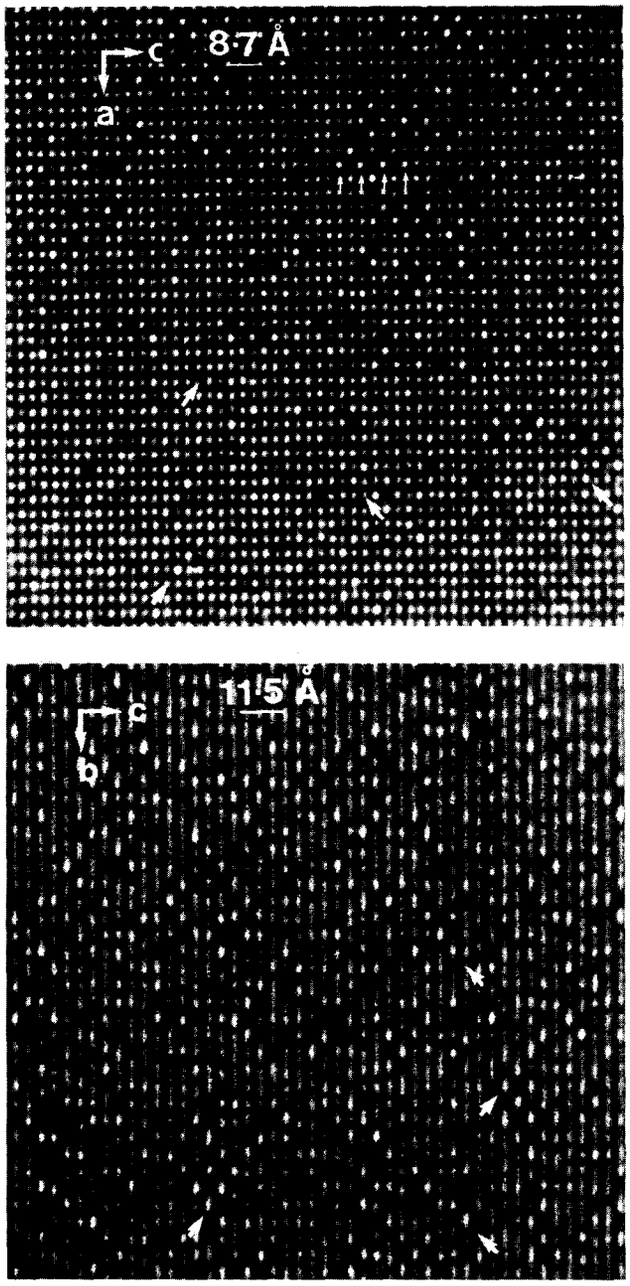

Fig. 2. 200 kV HREM images of 2:1 mullite: top, (0 1 0) plane; bottom, (1 0 0) plane.

building up an antiphase relationship. The pattern closely resembles those of Al-rich mullites ($x \geq 0{\cdot}48$)[9] but does not show long-range ordering. Vacancy arrangements in the (1 0 0) plane are characterized by preferred orientations along [0 1 2], [0 1 –2] and [0 0 1], resulting in an average direction parallel to [0 1 3] and [0 1 –3]. O_c columns with higher vacancy concentrations usually reveal distances of 1·5*b* and 5 to 6*c*.

Summarizing the HREM results, the oxygen vacancies in mullite form domains with higher defect concentrations and specific preferred directions. The domains are more or less statistically distributed in a disordered matrix. A schematic representation of the vacancy arrangements in the main crystallographic planes is presented in Fig. 5.

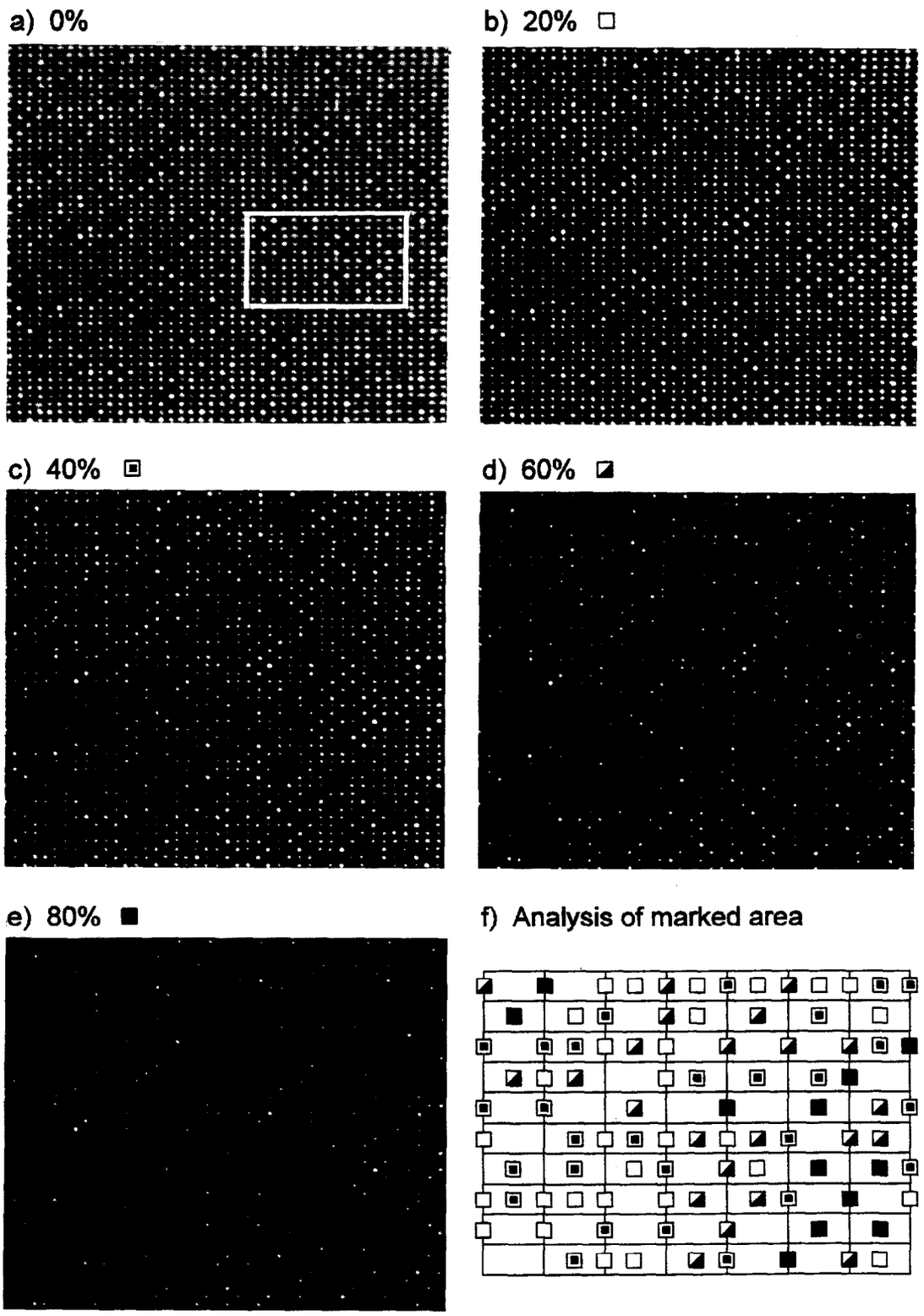

Fig. 3. Digital image processing of a 200 kV HREM image of the (0 1 0) plane. (a)–(e) Continuous filtering of dot greyscale in %. (f) Analysis of marked area in (a). *a*-Axis horizontal, *c*-axis vertical.

Although HREM investigations yield valuable information about preferred vacancy arrangements, one has to deal with some restrictions regarding the 3-D interpretation of the contrast patterns, since they are caused by a projection of the structure along the incident beam. However, the HREM results in the three main crystallographic directions give valuable parameters for two-dimensional (2-D) and 3-D videographic real structure simulations.

2-D Videographic Real Structure Simulations

The videographic method is a procedure for the determination of real structures and employs a

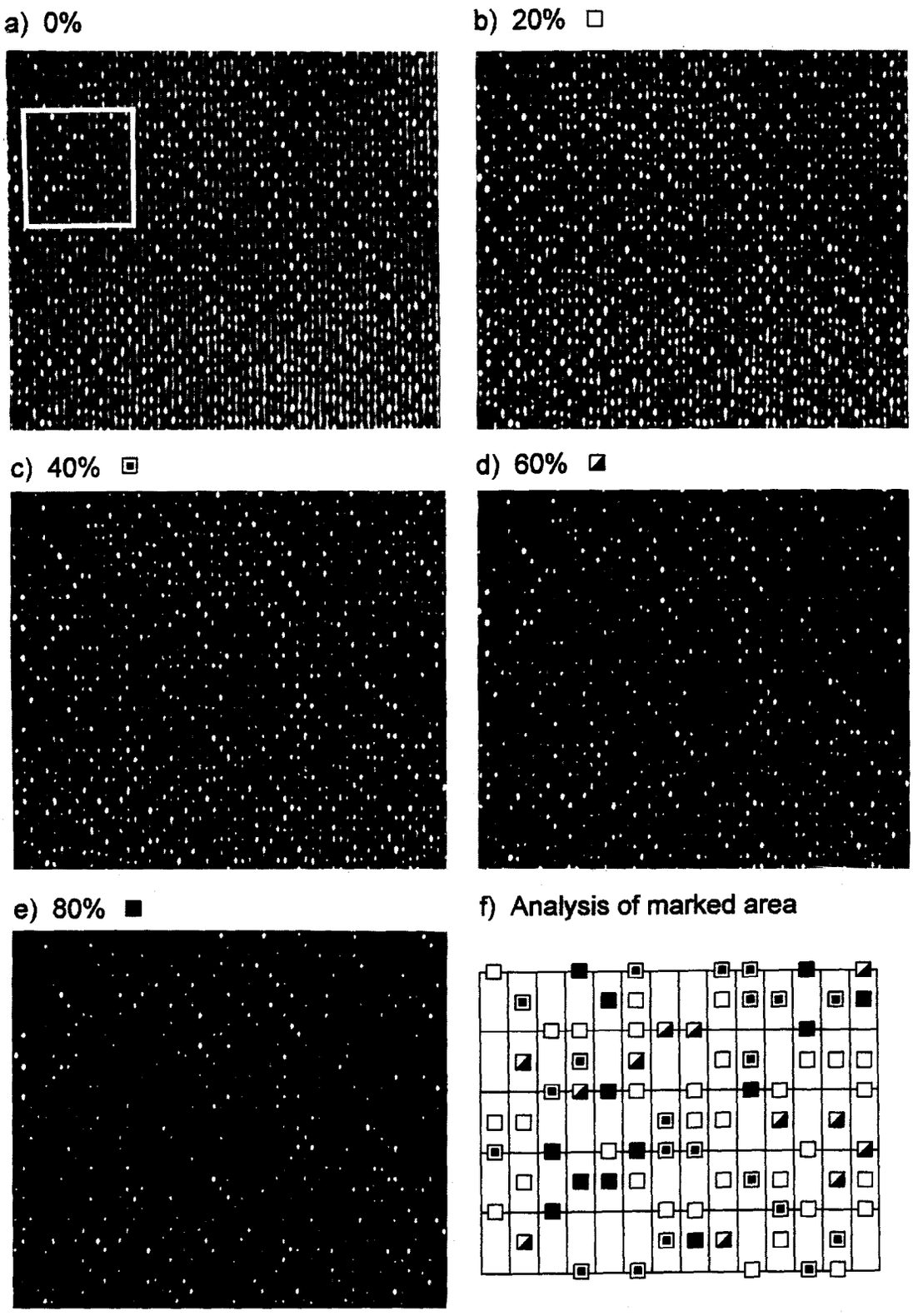

Fig. 4. Digital image processing of a 200 kV HREM image of the (1 0 0) plane. (a)–(e) Continuous filtering of dot greyscale in %. (f) Analysis of marked area in (a). *c*-Axis horizontal, *b*-axis vertical.

statistical mathematical approach and computer graphics to aid the interpretation of diffuse scattering from a disordered crystal.[22] The videographic method replaces atoms of different scattering power by pixels with varying grey levels. Instead of calculating the diffraction pattern by a time-consuming real space summation, the method offers the opportunity of using the fast FFT algorithm for Fourier transforming a real structure image (superstructure) which consists of structure variants, derived from the average structure.

Determinations of mullite average structure[23–29] revealed the space group *Pbam* with chains of edge-sharing AlO_6 octahedra along [0 0 1] which are crosslinked by (Si, Al) tetrahedral double chains [Fig. 6(a)]. Introduction of oxygen vacancies on

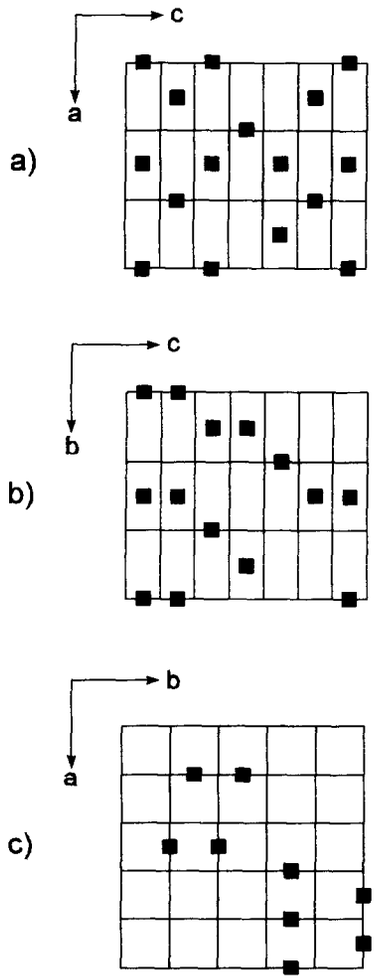

Fig. 5. Schematic representation of ordering schemes: (a) (0 1 0) plane; (b) (1 0 0) plane; (c) (0 0 1) plane.

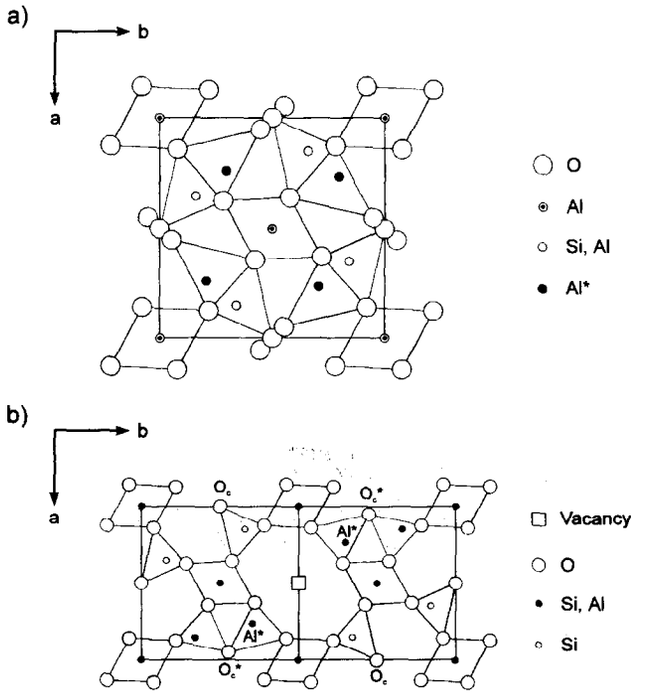

Fig. 6. (a) Average structure of mullite. (b) Atomic displacements around an oxygen vacancy.

O_c sites drives adjacent cations to occupy a new tetrahedral Al* site to preserve a fourfold coordination. Additionally, neighboured O_c atoms shift towards a less symmetric O_c* site [Fig. 6(b)]. According to Rahman,[22] the average structure can be described as a superposition of a number of structure variants which are usually derived by taking crystal chemical rules into account. For a deconvolution of the mullite average structure the following arguments were applied.

Si/Al–O_c* bond lengths of 0·173 and 0·178 nm lead to a tetrahedral occupation by Al, whereas 0·167 nm for the Si/Al–O_c bond gives an Si occupation of the tetrahedron in agreement with calculations of Padlewski *et al.*[20] Considering these rules and different O_c and O_c* occupations, it is possible to derive 34 structure variants from the mullite average structure which are represented in Fig. 7. Each four variants (1–4, 5–8, 9–12, 13–16) exhibit an oxygen vacancy on the same cell edge and different O_c/O_c* occupations on the remaining three edges. Numbers 17 to 32 are vacancy-free only with a variation on the O_c/O_c* sites. Variants 33 and 34 represent the silica-free ι-Al_2O_3 modification proposed by Saalfeld.[30] The distribution of the structure variants is performed using joint probabilities (nearest neighbours) and correlation vectors (next nearest neighbours, over next nearest) as described in more detail by Rahman[22] and Rahman and Rodewald.[31]

For the 2-D videographic real structure simulations, the following preferred vacancy arrangements, obtained from HREM investigations and interpretation of diffraction patterns,[11] were taken into consideration.

(0 0 1) plane: Linear arrangements along [1 0 0] and [0 1 0] occasionally separated by 1·5*b* and 1·5*a*, respectively.

(0 1 0) plane: Arrangements along [1 0 2] and [1 0 –2] with an incommensurate modulation of ≈1·5*a* and twofold periodicity along [0 0 1].

(1 0 0) plane: Arrangements along [0 1 2], [0 1 –2] and [0 0 1] with an incommensurate modulation of ≈1·5*b* and approximate fivefold modulation along [0 0 1].

Extended videographic simulations[32] with different structure variants represented by 8 × 8 and 16 × 16 pixel grids per structure variant yielded the preference of only a few correlation vectors to be responsible for the main features of the diffuse scattering in experimental X-ray diffraction patterns. The intensity distribution at higher scattering angles is mainly affected by an appropriate representation of the O_c/O_c* shift in the videographic structure image, whereas the Al/Si occupation of the tetrahedral sites only plays a negligible role. Figure 8 (top) shows a diffraction

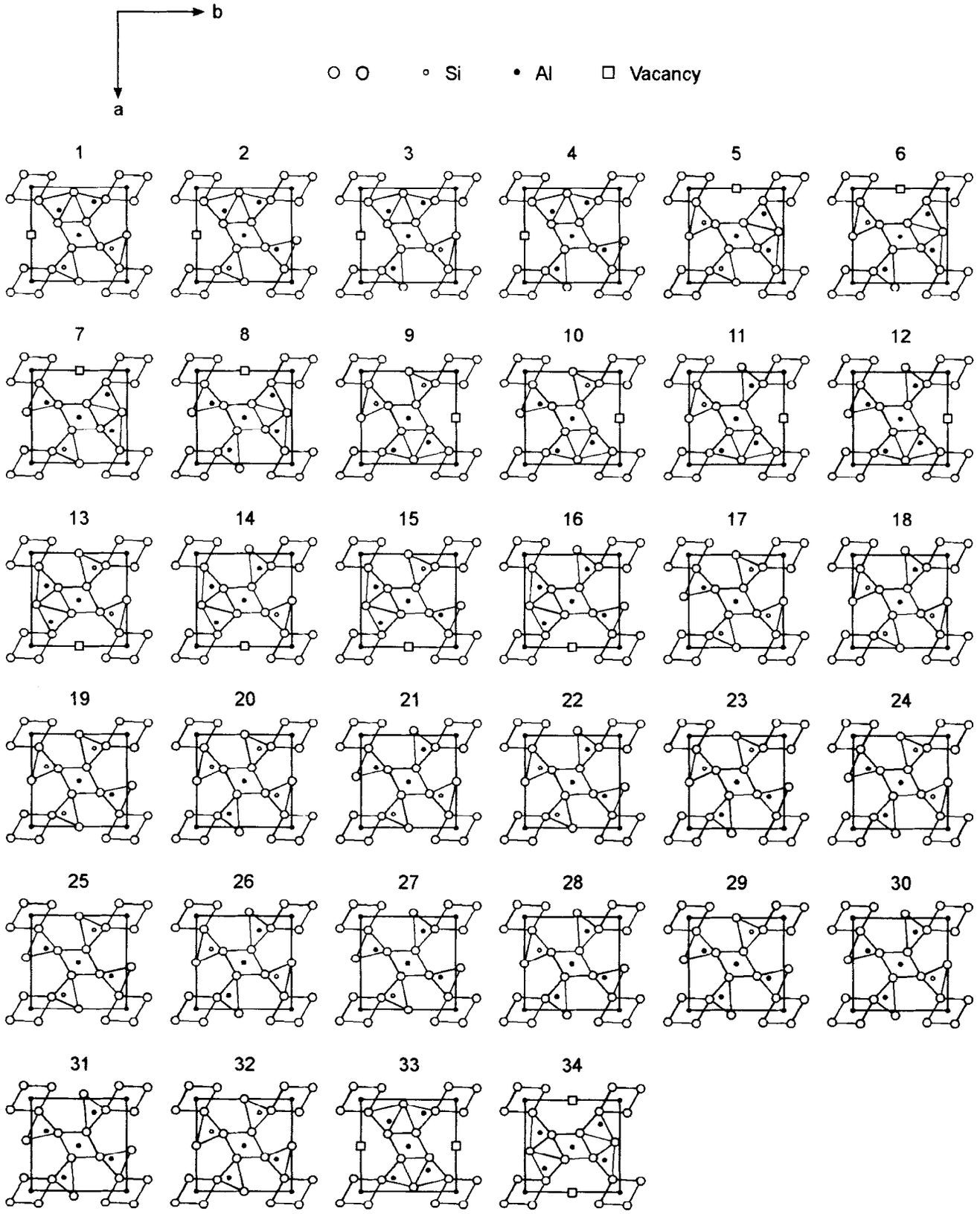

Fig. 7. 34 structure variants of mullite.

pattern of the $hk\frac{1}{4}$ plane which has been reconstructed from a digitized Weissenberg pattern with additional background correction and contrast enhancement of the weak diffuse scattering. Comparison with a Fourier transform [Fig. 8 (middle)] of the videographic structure image [Fig. 8 (bottom)] reveals good agreement because the application of a 16 × 16 grid allows the representation of all atomic positions with sufficient accuracy.

For an analysis of the structure image, the unit lengths of the correlation vectors (lmn) were chosen to be $l = \frac{1}{2}a$, $m = \frac{1}{2}b$ and $n = c$. An analysis of the simulation field shows a higher frequency of <310>, <130>, <330>, <020> and <200>

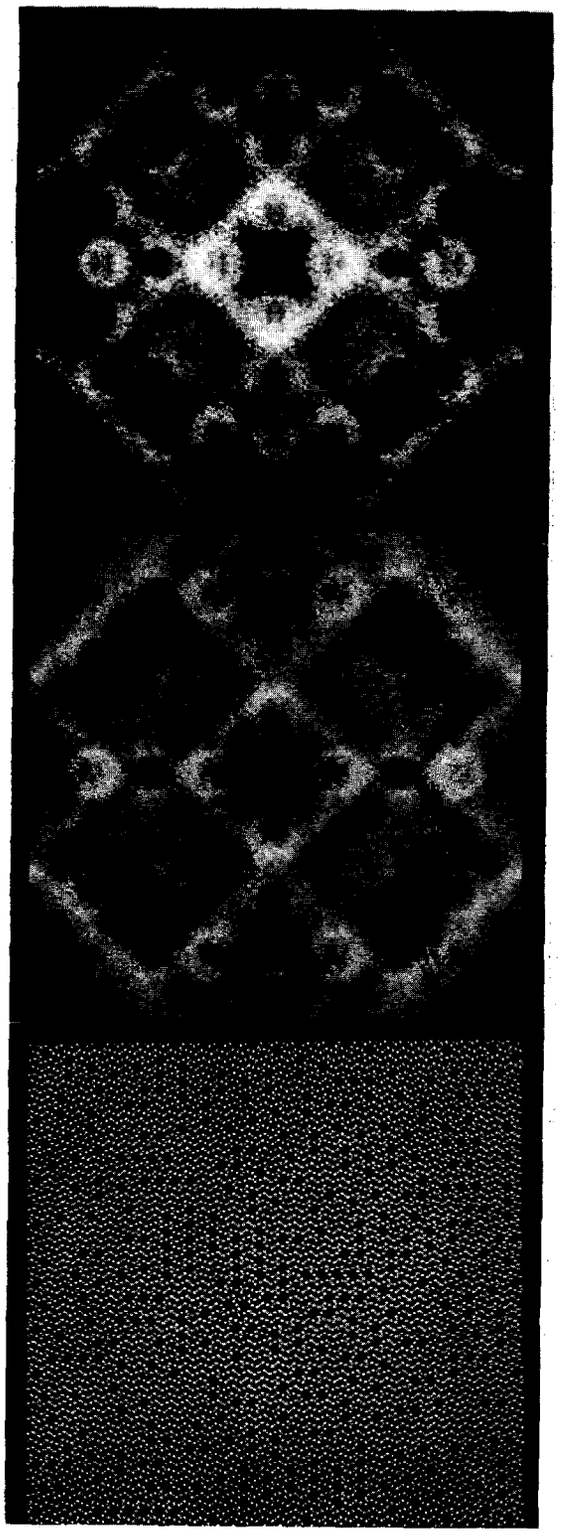

Fig. 8. 2-D videographic investigations of the $hk\frac{1}{4}$ plane: top, processed Weissenberg image; middle, Fourier transform of videographic structure image; bottom, small portion of videographic structure image. *b*-Axis horizontal, *a*-axis vertical.

short-range correlation vectors, where <3 3 0> results from a combination of <3 1 0> and <0 2 0> or <1 3 0> and <2 0 0>.

Further investigations confirmed that <1 3 0> and <3 1 0> are mainly responsible for the diffuse circles at the 01 and 10 positions [Fig. 8 (middle)], whereas the exact shape is caused by longer correlation vectors. Resulting from a combination of <1 3 0> and <3 1 0>, an equal number of <2 4 0>, <4 2 0>, <4 4 0>, <2 6 0>, <6 2 0>, <0 6 0> and <6 0 0> gives an exact circular shape of the diffuse scattering. In contrast, a higher frequency of <4 4 0> results in a rhombic form with edges along <1 1 0>*. Preferring <0 2 0> and <3 1 0> against <2 0 0> and <3 1 0> yields a diffraction pattern similar to the X-ray diffraction pattern of $hk\frac{1}{2}$.

Considering the above mentioned preferences, 2-D videographic real structure simulations were also performed for the (0 1 0) and (1 0 0) planes. By comparison, the satellite positions in the Fourier transforms of the videographic simulations are in close agreement with $h0l$ and $0kl$ electron diffraction patterns,[32] respectively. Analysis of the 2-D simulations yielded most frequent correlation vectors of <0 0 2>, <3 0 0>, <1 0 1>, <2 0 1>, <5 0 1> and <3 0 2> for the (0 1 0) plane. The (1 0 0) plane revealed a higher frequency of <0 3 0>, <0 2 2>, <0 0 5>, <0 2 3>, <0 0 6> and <0 1 3> correlation vectors.

Before proceeding with 3-D videographic simulations, some valuable information about the ordering scheme can be already obtained from the 2-D investigations. The 1·5-fold modulations along [1 0 0] and [0 1 0] in $h0l$ and $0kl$ diffraction patterns are caused by a preference of <1 3 0>, <3 1 0> and <3 3 0> correlation vectors. Furthermore, it can be assumed that the twofold period along [0 0 1] in $h0l$ patterns originates from more frequent <0 2 2> inter-vacancy correlation vectors which already appear in (1 0 0) HREM images as preferred arrangements along the <0 1 2> crystallographic directions (Fig. 2). Thus, a projection of the <0 2 2> vectors onto (0 1 0) results in a twofold period along [0 0 1].

3-D Videographic Real Structure Simulations

By comparing the frequencies of the correlation vectors in the 2-D simulations, a scheme of the 3-D vacancy distribution can be derived. The preferred vacancy arrangements along [1 0 2], [1 0 –2], [0 1 2] and [0 1 –2] (crystallographic directions) observed in HREM images can be achieved by a preference of the <1 1 1> correlation vector, in agreement with the 2-D simulation of the (0 1 0) plane with the high frequency of the <1 0 1>. The preference of <2 0 1> in the 3-D simulation corresponds to the <2 0 1> in the 2-D simulation of the (0 1 0) plane and – in projection on (1 0 0) – to a vacancy arrangement along [0 0 1] which appears in (1 0 0) HREM images. In addition, the correlation vectors <3 1 2>, <1 3 1>, <1 1 3> and <2 2 3> are preferred in the 3-D simulations.

After projecting the 3-D videographic simulation field along the main crystallographic directions, the correctness of the simulated structure model was tested by comparing its Fourier transforms with experimental diffraction patterns (Fig. 1). The Fourier transforms of the (0 1 0) and (1 0 0) planes are given in Fig. 9. The positions and intensities of the satellites are in close agreement to the experimental diffraction patterns of the $h0l$ and $0kl$ planes. It can be concluded that the input parameters for the simulation field resemble the vacancy distribution in 2:1 mullite. The most frequent 15 inter-vacancy correlation vectors determined by analysing the simulation field are presented in Table 1 together with those measured by Butler and Welberry.[21] Further calculations showed that slight changes in the frequencies and order of the correlation vectors do not influence the positions of the satellites but only have influence on the shape of the satellites and the intensity of streaks. It must be noted that the most frequent inter-vacancy vector <0 2 2> belongs to the second shell and plays an important role for the formation of the diffuse scattering in the $h0l$ and $0kl$ planes together with <3 3 0>, <3 1 0> and <1 3 0>. The correlation vector <0 2 2> can be obtained by a certain sequence of two <1 1 1> vectors (e.g. [1 1 1] followed by [–1 1 1] or [1 –1 1] followed by [–1 –1 1], etc.) However, it is unlikely that the occurrence of <0 2 2> is only caused by the combination of <1 1 1> since the frequencies of <1 1 1> and <0 2 2> are nearly the same.

Table 1. The most frequent 15 inter-vacancy vectors lmn ($l=a/2$, $m=b/2$, $n=c$) calculated from the 3-D simulation field [p = probability in %, a = short-range order parameter, a_{BW} = short-range order parameter determined by Butler & Welberry[21]]

lmn	p	a	a_{BW}
<0 2 2>	28·25	0·103	–
<3 1 0>	28·00	0·100	0·141
<1 1 1>	27·09	0·089	0·109
<2 0 1>	24·98	0·062	0·113
<3 3 0>	24·90	0·061	–
<1 3 0>	24·21	0·053	0·077
<4 0 1>	23·24	0·040	–
<1 1 3>	23·24	0·040	–
<0 4 0>	23·12	0·039	–
<0 0 4>	22·79	0·035	0·047
<1 3 1>	22·72	0·034	0·058
<2 2 2>	22·71	0·034	–
<2 2 3>	22·56	0·032	–
<6 0 0>	22·19	0·027	–
<3 1 2>	21·88	0·024	–

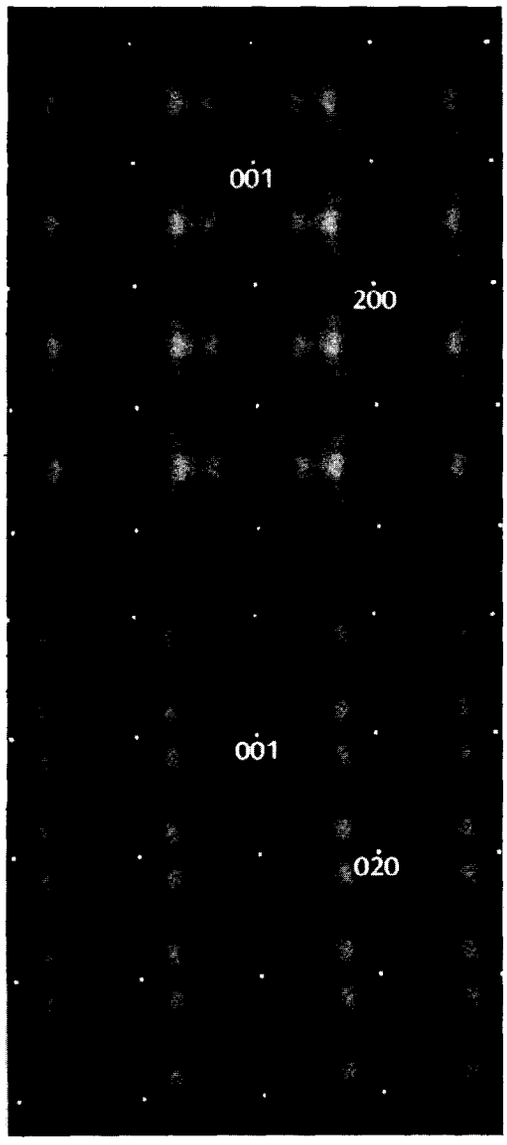

Fig. 9. Fourier transforms of the 3-D simulation field projected on (0 1 0) and (1 0 0).

Short-range order parameters (correlation vectors) are usually used to describe the real structure of intermetallic alloys above the critical temperature, T_c. In most cases, the first three short-range order parameters are adequate to describe the short-range ordered state. In mullite, with T_c above the melting point, the three shortest correlation vectors are not sufficient to describe the oxygen vacancy ordering scheme. In this case, higher order inter-vacancy correlation vectors (Table 1) are important for complete interpretation of the real structure.

Acknowledgement

The authors gratefully acknowledge financial support of the Deutsche Forschungsgemeinschaft.

References

1. Korekawa, M., Theorie der Satellitenreflexe. Habilitationsschrift, Universität München, 1967.

2. Böhm, H., Eine erweiterte Theorie der Satellitenreflexe und die Bestimmung der modulierten Struktur des Natriumnitrits. Habilitationsschrift, Universität Münster, 1977.
3. Schryvers, D., Srikrishna, M. A. & Thomas, G., An electron microscopy study of the atomic structure of a mullite in a reaction-sintered composite. *J. Mater. Res.*, **3** (1988) 1355–66.
4. Rahman, S. H. & Weichert, H.-T., Interpretation of HREM images of mullite. *Acta Crystallogr.*, **B46** (1990) 139–49.
5. Epicier, T., O'Keefe, M. A. & Thomas, G., Atomic imaging of 3:2-mullite. *Acta Crystallogr.*, **A46** (1990) 948–62.
6. Epicier, T., Benefits of high-resolution electron microscopy for the structural characterization of mullites. *J. Am. Ceram. Soc.*, **74** (1991) 2359–66.
7. Rahman, S. H., Interpretation of mullite HREM images using the potential-exchange-method. *Z. Kristallogr.*, **203** (1993b) 67–72.
8. Nakajima, Y., Morimoto, M. & Watanabe, E., Direct observation of oxygen vacancy in mullite, $1{\cdot}86Al_2O_3{\cdot}SiO_2$ by high resolution electron microscopy. *Proc. Jpn. Acad.*, **51** (1975) 173–8.
9. Ylä-Jääski, J. & Nissen, H.-U., Investigation of superstructures in mullite by high resolution electron microscopy and electron diffraction. *Phys. Chem. Minerals*, **10** (1983) 47–54.
10. Kahn-Harari, A., Abolhassani, S., Michel, D., Mazerolles, L., Portier, R. & Perez-Ramirez, J. G., Observation of ordering in silicon and germanium mullites. *J. Solid State Chem.*, **90** (1991) 234–48.
11. Paulmann, C., Rahman, S. H. & Strothenk, S., Interpretation of mullite HREM images along [0 1 0] and [1 0 0]. *Phys. Chem. Minerals*, **21** (1994) 546–54.
12. Saalfeld, H., The domain structure of 2:1-mullite. *N. Jb. Min. Abh.*, **134** (1979) 305–16.
13. Tokonami, M., Nakajima, Y. & Morimoto, N., The diffraction aspect and a structural model of mullite. *Acta Crystallogr.*, **A36** (1980) 270–6.
14. Welberry, T. & Withers, R. L., An optical transform and Monte Carlo study of the diffuse X-ray scattering in mullite $Al_2(Al_{2+2x}Si_{2-2x})O_{10-x}$. *Phys. Chem. Minerals*, **17** (1990) 117–24.
15. Rahman, S. H., Die Videographische Methode: Ein neues Verfahren zur Simulation und Rekonstruktion fehlgeordneter Kristallstrukturen. Habilitationsschrift, Universität Hannover, 1991.
16. Rahman, S. H., The real crystal structure of mullite. In *Mullite and Mullite Ceramics*, eds H. Schneider, K. Okada & J. A. Pask, Wiley and Sons, England, 1994, pp. 4–31.
17. Rahman, S. H. & Paulmann, C., Sauerstoffleerstellenverteilung in Mullit $Al_2[Al_{2+2x}Si_{2-2x}]O_{10-x}$. 25. *DGE Tagung in Darmstadt, Optik Supplement 4*, Vol. 88, 1991, Abstract 018.
18. Paulmann, C., Rahman, S. H. & Weichert, H.-T., Ordering scheme for oxygen vacancies in mullite. *Electron Microscopy EUREM92*, Granada, Spain, Vol. 2, 1992, pp. 445–6.
19. Butler, B. D., Welberry, T. R. & Withers, R. L., Oxygen vacancy ordering and the incommensurate structure of mullite. *Phys. Chem. Minerals*, **20** (1993) 323–32.
20. Padlewski, S., Heine, V. & Price, G. D., The energetics of interaction between oxygen vacancies in sillimanite: a model for the mullite structure. *Phys. Chem. Minerals*, **19** (1992) 196–202.
21. Butler, B. D. & Welberry, T. R., Analysis of diffuse scattering from the mineral mullite. *J. Appl. Crystallogr.*, **27** (1994) 742–54.
22. Rahman, S. H., The videographic method: a new procedure for the simulation and reconstruction of real structures. *Acta Crystallogr.*, **A49** (1993) 56–68.
23. Sadanaga, R., Tokonami, M. & Takeuchi, Y., The structure of mullite $2Al_2O_3{\cdot}SiO_2$ and relationship with the structures of sillimanite and andalusite. *Acta Crystallogr.*, **15** (1962) 65–8.
24. Burnham, C. W., The crystal structure of mullite. *Carn. I. Wash. Yb.*, **62** (1963) 158–62.
25. Burnham, C. W., Crystal structure of mullite. *Carn. I. Wash. Yb.*, **63** (1964) 223–7.
26. Durovic, S., Refinement of the crystal structure of mullite. *Chem. Zvesti*, **23** (1969) 113–28.
27. Angel, R. J. & Prewitt, C. T., Crystal structure of mullite a re-examination of the average structure. *Am. Mineral.*, **71** (1986) 1476–82.
28. Angel, R. J. & Prewitt, C. T., The incommensurate structure of mullite by Patterson synthesis. *Acta Crystallogr.*, **B43** (1987) 116–26.
29. Angel, R. J., McMullan, R. K. & Prewitt, C. T., Substructure and superstructure of mullite by neutron diffraction. *Am. Mineral.*, **76** (1991) 332–42.
30. Saalfeld, H., A modification of Al_2O_3 with sillimanite structure. *Transactions VIII International Ceramic Congress*, Copenhagen, (1962) pp. 71–4.
31. Rahman, S. H. & Rodewald, M., Simulation of short-range order in FCC-alloys. *Acta Crystallogr.*, **A51** (1995) 153–8.
32. Rahman, S. H., Strothenk, S. & Rodewald, M., Paper in preparation.